# Development of a $SnNb_2O_6$-Based Direct Z-Scheme Heterojunction A Novel Approach for Efficient Tetracycline Photocatalytic Degradation

Beiramzadeh, Zahra; Tanhaei, Mohammad; Li, Yixiang; Yang, Hui Ying; Hu, Jiangyong

**DOI**
10.1021/acsestwater.4c00888

**Publication date**
2025

**Document Version**
Final published version

**Published in**
ACS ES and T Water

ACS ES&T Water

pubs.acs.org/estwater

Article

# Development of a $SnNb_2O_6$-Based Direct Z-Scheme Heterojunction: A Novel Approach for Efficient Tetracycline Photocatalytic Degradation

Zahra Beiramzadeh, Mohammad Tanhaei, Yixiang Li, Hui Ying Yang, and Jiangyong Hu*

Cite This: *ACS EST Water* 2025, 5, 351−365

Read Online

ACCESS | Metrics & More | Article Recommendations | Supporting Information

**ABSTRACT:** With ever-increasing attention toward the removal of pharmaceuticals and personal care products (PPCPs), it is highly essential to study promising approaches for this purpose. We introduced a novel Z-scheme SNO-ACO photocatalyst developed via hydrothermal precipitation for degrading tetracycline (TC-HCl) under visible light. SNO-ACO-9% achieved 93% TC-HCl removal in 30 min, with a high pseudo-first-order kinetic rate (0.064 $min^{-1}$), 3.5 times faster than SNO, demonstrating exceptional efficiency and potential in environmental remediation, especially for antibiotic pollution. The photocatalyst's mechanisms involve enhanced light absorption and charge separation, which was facilitated through the addition of a strong oxidative photocatalyst, $Ag_2CO_3$, in a comparatively low amount in ratio to the parent reductive photocatalyst, $SnNb_2O_6$, without using a third agent as a charge mediator. Electron spin resonance (ESR) and scavenging experiments verified the formation of different reactive oxygen species and the Z-scheme heterojunction mechanism. This study will provide insight into using a more efficient system with heightened overall photodegradation activity in emerging contaminant removal.

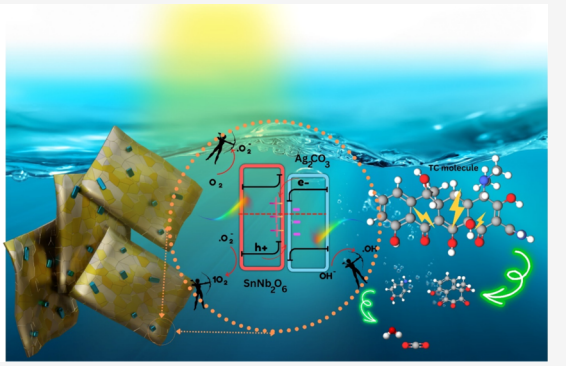


**KEYWORDS:** *photocatalysis, heterojunction, tetracycline, photodegradation, direct Z-scheme*



## 1. INTRODUCTION

The contamination of water environments by antibiotics and pharmaceuticals has emerged as a pressing global concern, posing serious threats to human health and aquatic ecosystems. The rampant misuse and illicit application of antibiotics in industries such as pharmaceuticals have resulted in an alarming increase in antibiotic pollution.[1−3] According to the United Nations Environment Programme (UNEP), human antibiotic consumption increased by 36% in this century and antibiotics used for livestock are anticipated to rise to 67% by 2030. Because degradation of these chemically stable structures has been proven to be low through conventional methods, the need for effective and sustainable water treatment methods to combat this pollution has never been more urgent.[4,5] Photocatalytic technology based on semiconductors has emerged as a highly promising and extensively studied solution for water treatment.[6,7] According to Scopus data, the number of publications in this field throughout 2018−2023 is 2.2-fold higher comparing to the time frame of 2012−2018. This technology harnesses the power of sunlight/visible light to generate photoexcited holes and electrons within the semiconductor material. Under light illumination, reactive oxygen species (ROS) initiate a potent oxidative process that effectively degrades contaminants.[8,9] Despite significant advances in photocatalyst development, it is challenging for a single photocatalyst to fulfill all criteria due to different limitations. Narrow-band-gap photocatalysts face issues with the recombination of photogenerated carriers, while wide-band-gap ones struggle to generate photogenerated electrons and holes effectively, leading to a reduced photocatalytic performance.[10] Low photoresponse ability, poor electron ($e^-$) and hole ($h^+$) transfer and quantum efficiency, and inadequate stability and lifespan are the most significant issues associated with a single-component photocatalyst system.[11] Hence, the search for photocatalysts exhibiting high activity, broad-spectrum absorption, efficient carrier transfer, and long-term stability is essential for applications in energy and the environment.

Heterojunction systems can enhance a single photocatalyst system by the following:

Received: September 15, 2024
Revised: November 27, 2024
Accepted: November 27, 2024
Published: December 17, 2024

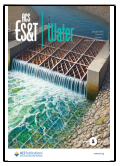

1. Enhanced light absorption, where materials with small band gaps or highly absorbent molecules can strengthen the performance of large-band-gap semiconductors.
2. Improved charge separation and transport, facilitated by structures like p−n junctions or Schottky junctions, which effectively separate electron−hole pairs.
3. Incorporation of cocatalysts, which reduce redox overpotentials at active sites.
4. Increased stability, as surface passivation protects the semiconductor from degradation. Factors such as chemical corrosion, catalyst deactivation from solution contaminants, and morphological or compositional changes during the photocatalytic process can significantly impact the performance. However, integrating multiple components holds promise for reducing semiconductor damage and improving overall stability.[11,12]

The Z-scheme system has garnered significant attention as an efficient approach to enhance the photocatalytic removal activity of a single catalyst. This mechanism incorporates the utilization of electrons ($e^-$) and holes ($h^+$) in the higher conduction band (CB) of the more reductive photocatalyst and the lower valence band (VB) of the more oxidative photocatalyst, ensuring strong reduction and oxidation capabilities.[13] By minimizing charge carrier recombination, Z-scheme systems surpass other photocatalytic composites in degrading organic pollutants.[14−16] This tandem configuration optimizes energy distribution, facilitating efficient charge transportation and suppressing electron−hole recombination, ultimately boosting the photoactivity of the composite.[17] Under visible-light irradiation, both heterojunction photocatalysts generate electron−hole pairs, leading to the production of oxygen-containing free radicals, such as $^{\bullet}OH$ and $^{\bullet}O_2^-$, further enhancing the photodegradation efficiency and rate.[18,19]

One of these reductive photocatalysts is $SnNb_2O_6$ (SNO), which has a band gap of 2.2−2.4 eV[20,21] with high visible-light activity and stability. Tin niobates were first synthesized and examined by Cruz et al.[22] However, their photocatalytic properties had not been explored until Hosogi et al. conducted an in-depth study on the photocatalytic $O_2$ and $H_2$ evolution using $SnNb_2O_6$ synthesized through various processes.[20] Additionally, the group was the first to investigate $SnNb_2O_6$ synthesized by both solid-state reactions and $SnCl_2$-treated methods.[23]

The most recent forms of SNO nanosheets are composed of two edge-sharing $Nb^VO_6$ octahedra with $Sn^{2+}$ inserted between planes with a two-octahedron thickness. Because of the CB and VB band edge positions, they can be applied for many applications, such as water splitting and organic contaminant degradation.

Two distinct starting materials, including commercial SnO and $Sn_3O_2(OH)_2$, were used as Sn sources to prepare $SnNb_2O_6$ photocatalysts in the study by Hosogi et al.[20] $SnNb_2O_6$ prepared with the SnO precursor exhibited a greater amount of $Sn^{4+}$ compared to the one prepared with $Sn_3O_2(OH)_2$; although the total $Sn^{4+}$ content was relatively small, the $Sn^{4+}$ ion replaces $Nb^{5+}$ ions, based on the ionic radius and oxidation state. Research has indicated that some $Nb^{5+}$ ions in tin niobates can be substituted by $Sn^{4+}$ ions. The $Sn^{4+}$ species acts as an electron trap beneath the conduction band, leading to a reduced photocatalytic performance. The study suggested that valence band regulation via $Sn^{2+}$ and minimizing the creation of $Sn^{4+}$ impurities and grain boundaries could improve photocatalytic activity.

Ma et al. applied this photocatalyst in junction with $WO_3$, which outperformed each of them in Rhodamine B decomposition.[24] Also, another Z-scheme heterojunction of SNO and BiOCl has been investigated to remove benzocaine, and it showed a superior performance in its junction form.[25] To the best of our knowledge, to date, other Z-scheme SNO-based heterostructures have not been reported in literature.

$Ag_2CO_3$ (ACO) is a widely utilized cocatalyst in photocatalysis, known for its exceptional optical performance and appropriate band gap energy of 2.3 eV.[26−28] Its high potential valence band edge (+2.92 eV vs NHE) makes it a preferred component in Z-scheme heterojunctions, enabling a robust oxidation potential and an efficient transfer of photoinduced charges.[29] Combining $Ag_2CO_3$ with other materials has yielded impressive results; for instance, the modification of g-$C_3N_4$ with $Ag_2CO_3$ and graphene oxide produced a highly stable Z-scheme photocatalyst with remarkable stability.[29] Additionally, the formation of a unique double Z-scheme system, AgBr/$CeO_2$/$Ag_2CO_3$, demonstrated superior photocatalytic activity in comparison to each individual photocatalyst.[26] Considering its well-matched band positions with $SnNb_2O_6$, $Ag_2CO_3$ could potentially be proven to be a rational choice for cocatalysis, facilitating the accelerated separation of photoinduced charges in this heterojunction.

In this work, for the first time, we introduced a novel binary SNO/ACO direct Z-scheme photocatalytic system synthesized for antibiotic oxidation. We fabricated this binary material through a hydrothermal precipitation process. This composite structure, which was produced without the addition of any mediator or charge transfer agent, exploits the distinct role of SNO as 2D nanosheets with a superior absorption catalytic effect, and we incorporated ACO as powerful structures to enhance light absorption and separating charge carriers in the individual SNO system via the Z-scheme transfer path. Visible-light photocatalytic removal activity was evaluated by using tetracycline (TC-HCl) as the target pollutant. This study showed that the produced binary photocatalyst outperformed other equally studied binary or tertiary structures in pharmaceutical removal with a high kinetic rate in a shorter reaction time. The results of this investigation provide valuable perspectives for enhancing forthcoming dual direct Z-scheme photocatalysts aimed at tackling antibiotic pollutants in environmental remediation.

## 2. MATERIALS AND METHODS

**2.1. $SnNb_2O_6$/$Ag_2CO_3$ Synthesis.** The SNO/ACO binary composite was synthesized using a coprecipitation reaction.[31] Initially, a specific amount of prepared SNO was dispersed in 35 mL of ultrapure water through stirring for 1 h. (Details of the SNO synthesis procedure are provided in the Supporting Information.) Subsequently, the desired amount of $AgNO_3$ was uniformly dispersed by sonication for 30 min in the above solution. Concurrently, a stochiometric amount of $Na_2CO_3$ was dissolved in 30 mL of ultrapure water and gradually added to the solution. The mixture was stirred in the absence of light for 60 min. The resulting product was collected through the centrifugation process and washed few times with deionized water and ethanol, forming the SNO/ACO composite. The acquired specimens were labeled as SNO-ACO-*X*; the number *X* is corresponding to the percent mass of $Ag_2CO_3$ within the


https://doi.org/10.1021/acsestwater.4c00888
ACS EST Water 2025, 5, 351−365

**Scheme 1. Cartoon Showing the Hydrothermal Process of SNO 2D Nanosheet Synthesis Subsequently Used to Prepare the SNO/ACO Composite through Coprecipitation (a) Photochemical Setup Using a Reactor of 50 mL TC-HCl Solution (10 mg/L) Equipped with a Water Jacket for Cooling the System and Keeping a Stable Temperature and Photocatalyst dosage of 1 g/L. The Light Source for Photocatalyst Activation is a 300 W Xenon Lamp with a 400 nm Cutoff (b)**

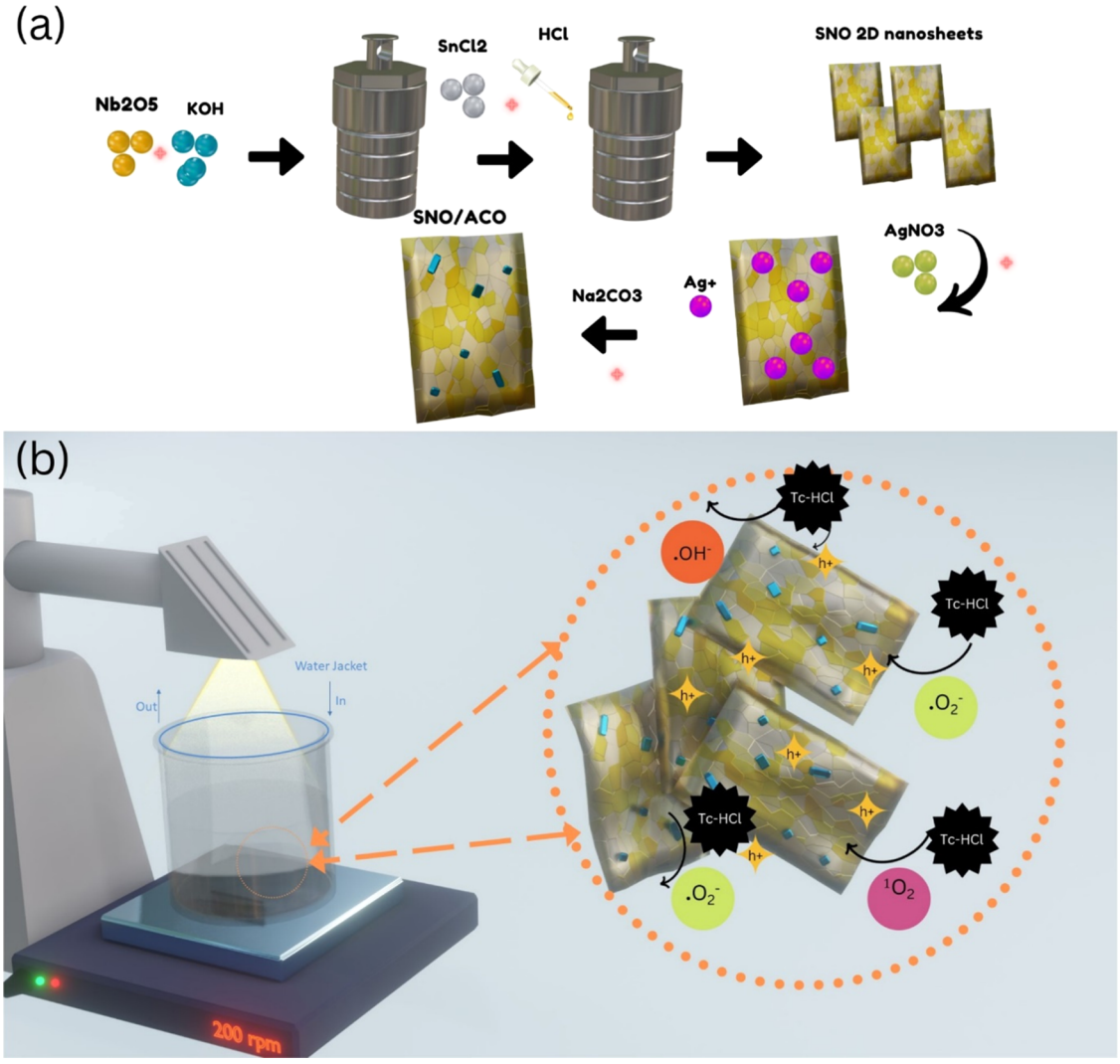


entire composite, and the synthesis process is illustrated in Scheme 1a. It is noteworthy to mention that SNO-ACO-9 (among SNO-ACO-1, SNO-ACO-3, SNO-ACO-5, SNO-ACO-9) was chosen as the optimal composite in this study. For comparison, ACO was prepared in a similar manner, with no SNO precursor addition.

A detailed experimental section is provided in the Supporting Information.

## 3. RESULTS AND DISCUSSION

The Z-scheme photocatalytic system has demonstrated significant improvements in photocatalytic reactions on account of the merits in light absorption, highly robust redox potentials, and isolated reductive and oxidative active sites, which make this system advantageous to others. In this study, we successfully prepared SNO catalysts with a flowerlike structure with the diameter of approximately 4 to 5 $\mu$m and thickness of 10 nm,[32] which was shown in the scanning electron microscopy (SEM) (Figure S1a) and transmission electron microscopy (TEM) images in Figures 1a and S2a,b. ACO nanoparticles (SEM image, Figure S1b) with higher light absorption and oxidation ability successfully attached to the nanosheet 2D SNO structure, as shown in TEM images (Figure 1b). SNO with a nanosheet design improves the surface area and effectively boosts electron and hole transfer.[33] Evidently, the presence of a large and well-defined contact interface between ACO nanoparticles and the SNO nanosheet is distinct. Moreover, the high crystallinity of both ACO and SNO is evident from the clearly discernible lattice spacings. The lattice fringes, spaced at 0.23 nm, align well with the (031) planes of ACO.[31,34] Additionally, the lattice spacing of 0.3 nm corresponds to the (−311) plane and that of 0.35 nm to the (−111) plane of SNO.[30]

$N_2$ adsorption−desorption isotherms and the Barrett−Joyner−Halenda (BJH) method evaluated the BET surface area and pore structure of the samples, revealing type IV patterns with H3 hysteresis loops, indicative of slitlike mesoporous structures. The SNO-ACO-9 composite had a slightly smaller surface area (28.76 $m^2/g$) than pure SNO (31.33 $m^2/g$), suggesting that the surface area alone may not significantly enhance the photocatalytic performance (additional information provided in Figure S3 and Table S1).


https://doi.org/10.1021/acsestwater.4c00888
ACS EST Water 2025, 5, 351−365

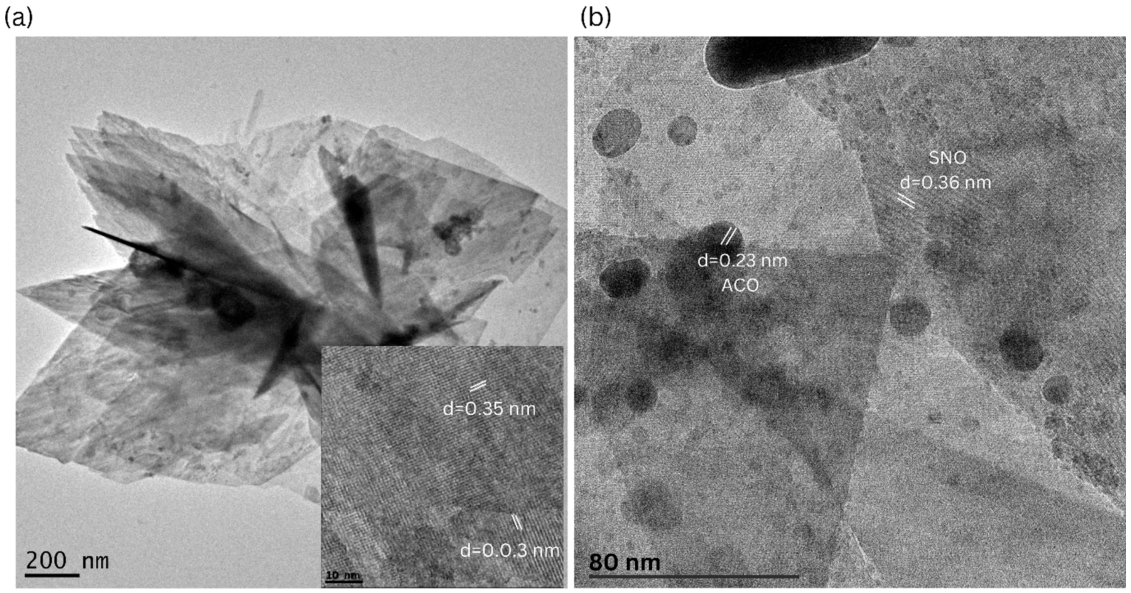


**Figure 1.** HRTEM images of SNO (a) and SNO-ACO-9 (b). The nanostructured design enhances the surface area and promotes efficient electron and hole transfer. The distinct contact interface between ACO nanoparticles and SNO nanosheets highlights their high crystallinity, as evidenced by observable lattice spacings aligned with specific crystallographic planes.

In order to examine the surface characteristics of photocatalysts and the compositional state associated with the surface elements and bonding configuration of the binary composite, XPS spectroscopy was employed. The Sn 3d spectrum (Figure 2a) displays two peaks at 486.5 and 494.9 eV, consistent with the Sn $3d_{5/2}$ and Sn $3d_{3/2}$ orbitals of $Sn^{2+}$. In the Nb 3d spectrum (Figure 2b), peaks at 207.260 and 210.0 eV confirm the presence of $Nb^{5+}$.[3535] Regarding the Ag 3d spectrum (Figure 2c), peaks at 368.4 and 374.4 eV correspond to Ag $3d_{5/2}$ and Ag $3d_{3/2}$, respectively, confirming the presence of $Ag^{+}$ species in the composite.[36] Notably, Ag 3d peaks overlapped with Nb 3p emission peaks, which was confirmed in previous reports.[37] In the C 1s spectrum (Figure 2d), two peaks at 284.8 and 288.9 eV are attributed to the C−C bond and adventitious carbon and the C═O bond of ACO. The observed peak at 286.4 eV could potentially be attributed to the absorbed carbon contamination during the synthesis process.[38,39] The O 1s spectrum (Figure 2e) exhibits a peak at 531.6 eV, representing the O−H bond, while the peak at 530.3 eV corresponds to lattice oxygen, the $O^{2-}$ anion of the SNO crystalline structure. Significantly, the peaks corresponding to Ag 3d, Sn 3d, Nb 3d, and O 1s observed in the SNO-ACO-9 sample exhibit a noticeable shift toward higher binding energies. This shift suggests that a strong interfacial interaction is occurring within the heterojunction. This interaction likely arises from potential electron transfer by the close contact between ACO and SNO nanosheets.

Having conducted the morphological and compositional characterization experiments and more, which are elaborately explained in the ensuing sections, we evaluated the prepared Z-scheme system in the environmental application in the next following step. The Z-scheme system is potentially influential in the kinetic rate of the contaminant removal and its oxidation mechanism in comparison to the individual photocatalyst system.[40] In our system, the target pollutant of TC-HCl was used to assess the photocatalytic capabilities of the fabricated materials under visible-light exposure. Before initiating the photocatalytic process, the adsorption−desorption equilibrium was established by stirring continuously for 30 min in the absence of light. As depicted in Figure 3a, the prepared photocatalysts adsorb TC-HCl after a 30 min reaction in the absence of light due to the nanosheet structure and high surface area of SNO and the heterostructure creating more active sites for TC-HCl molecules to bind. SNO-ACO-9 absorbed 21% of TC-HCl in the dark, which is slightly lower than the amount absorbed by pure SNO, which could be due to ACO compacting the structure of SNO by entering its macro- and mesopores and slightly reducing the surface area. This effect was substantiated in the X-ray diffraction (XRD) analysis (Figure S4) and based on Scherrer and Williamson−Hall equations (eqs S4−S6), the crystalline size of SNO decreased by 6%, confirming that the interaction and attachment of ACO to SNO is the driving force for the change in the crystalline size (further explanation on XRD analysis is provided in the Supporting Figure S4).[41]

SNO demonstrates the least effective degradation, with only 60% TC-HCl removed after 30 min of irradiation. Notably, no significant decrease in the TC-HCl concentration is observed without photocatalysts under visible light, indicating a negligible direct photolysis of TC-HCl. The TC-HCl photodegradation efficiency improves to more than 90% in the presence of the ACO nanocomposite. Upon being activated by the light source, SNO-ACO-9% rapidly degraded TC-HCl under visible-light exposure. Remarkably, SNO-ACO-9 outperforms others in visible-light-responsive photodegradation (Table S2), achieving a 91% removal of TC-HCl within 30 min. Figure S5 depicts the photodegradation rate of the photocatalysts according to the pseudo-first-order kinetic rate (eq S2), indicating the highest removal rate attributed to SNO-ACO-9% (0.064 $min^{-1}$). This increase in the degradation performance is due to the amount of ACO in the composite structure, which helps with more interfacial area for charge separation and the facile transfer of electrons and holes. This exceptional performance can also be attributed to the heterojunction's excellent light-absorbing capability, which is supported by optical property analysis by DRS. The results of


https://doi.org/10.1021/acsestwater.4c00888
ACS EST Water 2025, 5, 351−365

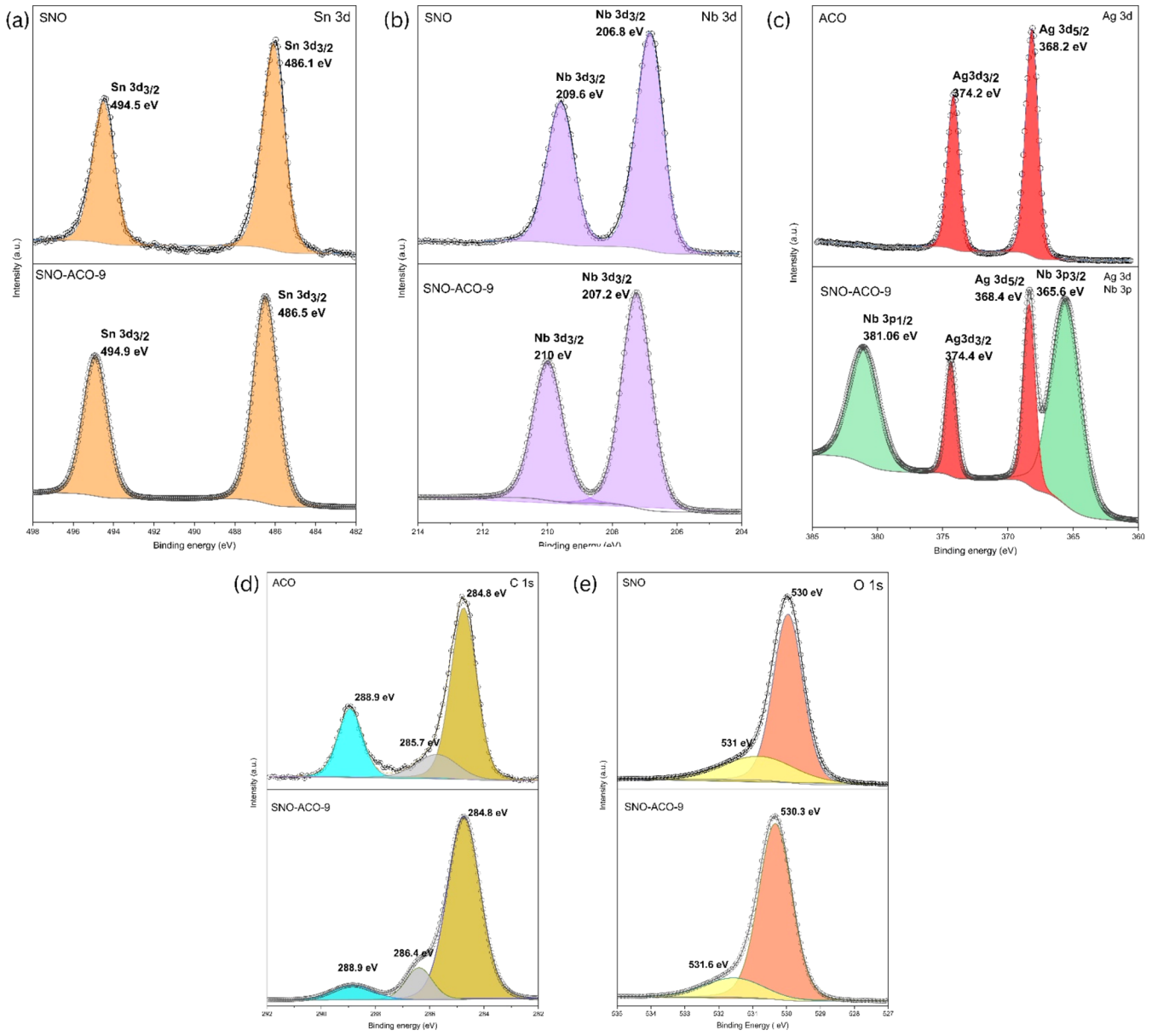


**Figure 2.** X-ray photoelectron spectroscopy (XPS) spectra of SNO-ACO-9: Sn 3d (a), Nb 3d (b), Ag 3d (c), C 1s (d), and O 1s (e). XPS spectroscopy reveals the surface characteristics and compositional states of the photocatalysts. Peaks in Sn 3d, Nb 3d, Ag 3d and O 1s spectra of the SNO-ACO-9 sample shift toward higher binding energies, indicating a strong interfacial interaction, potentially facilitating electron transfer between ACO and SNO nanosheets.

DRS analysis showed that the SNO-ACO-9% heterojunction displays distinctive optical absorption features corresponding to pure SNO and ACO (Figure S6), generating a red-shifted SNO adsorption spectrum by introducing ACO in the material, suggesting a substantial enhancement in the visible-light response of SNO upon combination with ACO. The heightened visible-light absorption of SNO-ACO-9 generates more electron−hole pairs, while its well-defined crystallinity hinders electron−hole pair recombination. The change in the lattice structure could potentially enable the facile transport of electrons, holes, and electrolyte ions within the abundant space, expediting the photocatalytic degradation of TC-HCl under visible-light irradiation.

The variation in the photodegradation efficiency is predominantly influenced by the interplay between tetracycline p$K_a$ values under different pH conditions and the isoelectric point (IEP) of SNO-ACO-9%. The influence of pH on the photocatalytic degradation of TC-HCl by SNO-ACO-9% was systematically investigated across a range of pH values from 4 to 10, given that pH is a crucial factor impacting photocatalytic activity. The pH range of 4−10 was selected for analysis due to tetracycline's p$K_a$ values (3.3, 7.6, and 9.6), which determine its protonation and charge states. These p$K_a$ values influence tetracycline's behavior in different pH environments, affecting its removal efficiency in photocatalytic or photoelectrochemical processes.[42] As depicted in Figure 3b, after 40 min of irradiation, with the increase in pH from 4 to 5.5, the efficiency increased from 89 to 93% and the highest removal efficiency happened at pH 5.5; there is a slight decrease in removal from pH 5.5 to 8. As the pH further increased to 10, the photodegradation efficiency of TC-HCl further reduced to 85%. The results clearly indicate that even though pH could be


https://doi.org/10.1021/acsestwater.4c00888
ACS EST Water 2025, 5, 351−365

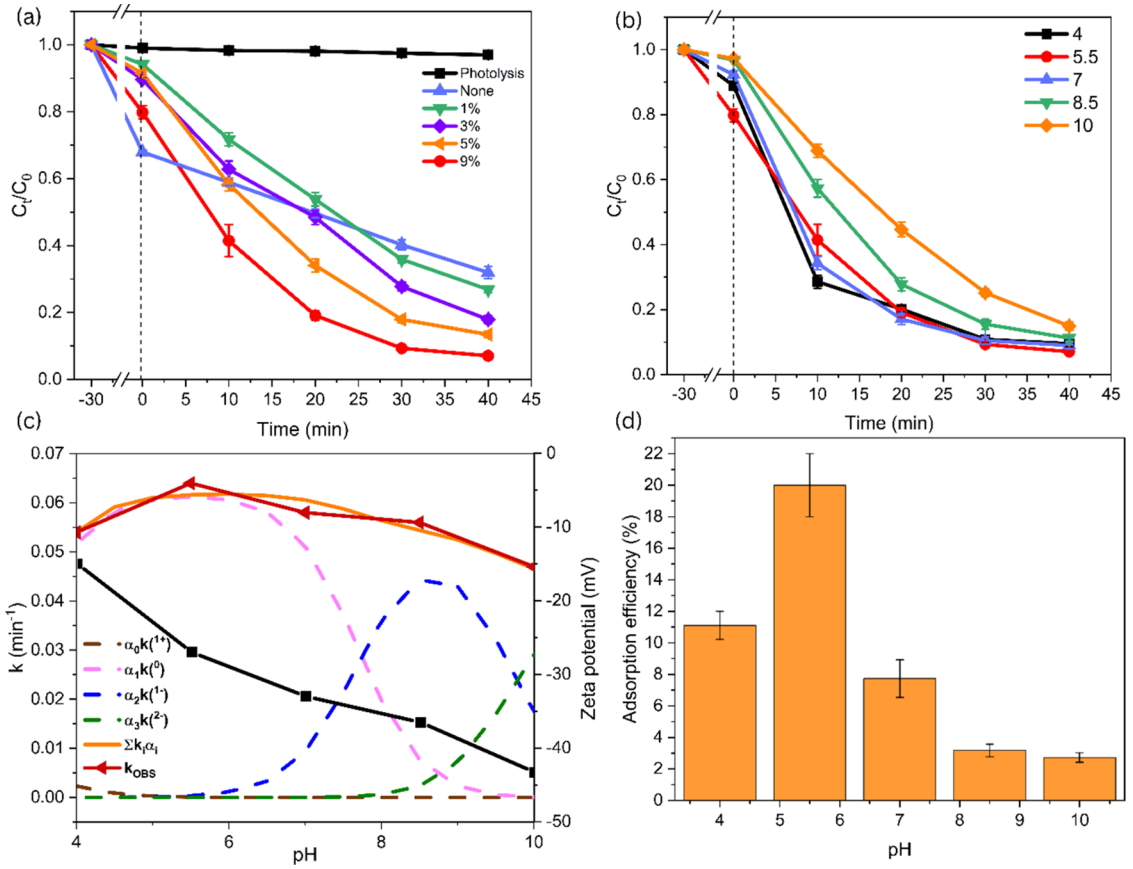


**Figure 3.** Photodegradation graphs of TC-HCl by different photocatalysts (the percentage is indicative of the ACO mass ratio to the mass of the composite, [PC] = 1 g/L, pH 5.5, TC = 10 mg/L (a); the effect of different pH values on TC removal (b); the TC-HCl dissociate-based photodegradation rate and their changes according to pH values and photocatalyst surface charge (c); and the adsorption of TC-HCl in dark in different pH conditions (d)).

an influential factor in the photoactivity of SNO-ACO-9%, the physical and chemical stability of the material in lower and higher pH values would assist in the photodegradation performance with less fluctuations.

Additionally, we examined the adsorption of TC-HCl onto the heterojunction at different pH levels in the absence of light. As presented in Figure 3d, under acidic conditions with pH 4−5.5, the adsorption of TC-HCl onto the material was increased from 11 to 20% after a 30 min reaction. This could be attributed to the electrostatic attraction between the more negative surface (−29 mV) of the material and the zwitterionic form. In more acidic conditions, the interaction between more positively charged SNO-ACO-9 (less negative) and cationic TC is a deterrent and resulted in weak TC adsorption on the SNO-ACO-9 surface. Furthermore, the adsorption efficiency of TC-HCl decreased with the increase in pH from 7 to 10. This decline could be due to an increase in the presence of the deprotonated form of TC-HCl in water and its electrostatic repulsion between more negatively charged SNO-ACO and anionic TC-HCl, which weakened their interaction and resulted in lower TC-HCl adsorption on the SNO-ACO surface. This pattern of adsorption aligns with the photodegradation trends of TC-HCl at varying pH levels.

The variation in the photodegradation efficiency is predominantly influenced by the interplay between tetracycline p$K_a$ values and the isoelectric point (IEP) of SNO-ACO-9%. Notably, TC exhibits p$K_a$ values of 3.3, 7.6, and 9.6. This implies that TC carries a positive charge ($TC^+$) at pH values below 3.3 due to the protonation of amino groups. Between pH values of 3.3 and 7.6, TC adopts a zwitterionic form ($TC^{\pm}$). Importantly, the isoelectric point ($pH_{IEP}$) of SNO-ACO-9% is measured at 3.5. Consequently, it is negatively charged at pH values higher than 3.5. Between pH values of 7.6 and 9.6, TC assumes an anionic form ($TC^-$). And even higher basic conditions lead to more deprotonation and formation of the TC dianion ($TC^{2-}$). The $\zeta$-potential result supports the lower adsorption of TC onto SNO-ACO-9% at pH 4 and when the pH climbs to 5.5, it accelerates the adsorption and photodegradation because more zwitterionic TC is available to react with the reactive oxygen species (ROS) on the photocatalyst's surface. The deprotonated form of TC is more electron-rich and susceptible to oxidation than the protonated form. However, at pH values exceeding 9.6, which surpasses TC's p$K_{a_3}$, fully deprotonated TC (TC dianion) struggles to interact with negatively charged SNO-ACO (with a $\zeta$-potential <−40 mV), resulting in a decline in the photocatalytic degradation rate of TC at elevated levels like pH = 10.

The photodegradation rate of TC by SNO-ACO-9% at different pH levels ($k_{obs}$) quantified using the pseudo-first-order rate equation is depicted in Figure 3c. The TC photodegradation rate ($k_{obs}$) ranges from 0.054 to 0.064 min$^{-1}$ at pH 4−5.5 and then decreases with a pH increase to 8.5. However, the $k_{obs}$ markedly decreases to 0.047 min$^{-1}$ with further increases in pH to 10. Notably, TC dissociation into species depends highly on the pH of the solution, and as such,


https://doi.org/10.1021/acsestwater.4c00888
ACS EST Water 2025, 5, 351−365

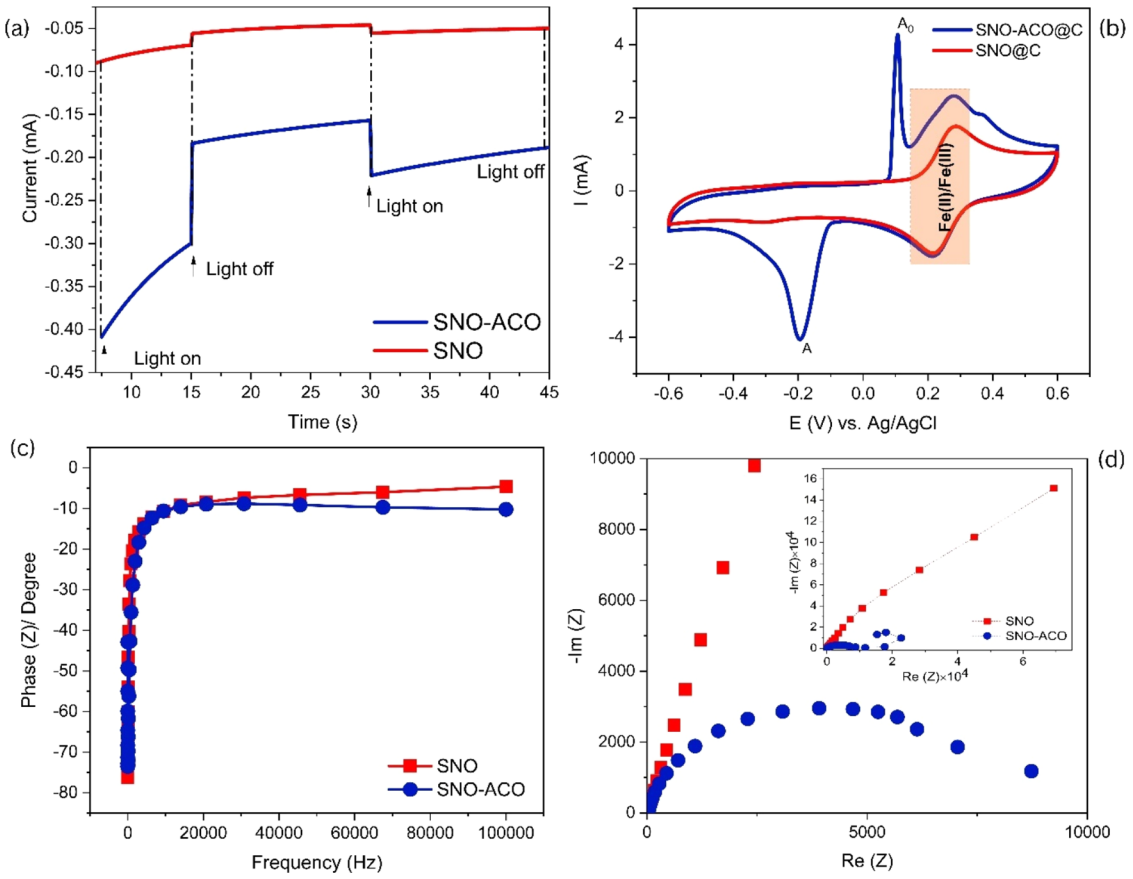


**Figure 4.** Transient photocurrent response in 0.5 M $Na_2SO_4$, −0.6 V vs Ag/AgCl (a), cyclic voltammogram graphs in 0.5 M KCl/5.0 mM ($K_3[Fe(CN)_6]/K_4[Fe(CN)_6]$) solution (b), Bode-phase plots (c), and EIS Nyquist plot (the inset figure is the associated zoom-out graph) (d).

the $k_{obs}$ for TC photodegradation can be expressed as a function of $TC^+$, $TC^{\pm}$, $TC^-$, and $TC^{2-}$ rate constants and the molar fraction of each species, which are described in Text S1.[43] The dissociation constants of TC, denoted as $K_{a_0}$, $K_{a_1}$, $K_{a_2}$, and $K_{a_3}$, were taken into account. As revealed in Figure 3c, it is evident that the prevailing species is the zwitterionic form of TC, exhibiting the highest rate of 0.062 $min^{-1}$, followed by the anionic form with a rate of 0.054 $min^{-1}$ and the dianionic form at 0.043 $min^{-1}$. Finally, the lowest degradation rate is ascribed to cationic TC with a rate of 0.014 $min^{-1}$.

The effect of the ionic strength, NOMs, and photocatalyst dosage on TC-HCl has been elaborately described in the Supporting Figures S7−S9. The result of these experiments indicated that with an increase in the ionic strength and HA concentration, the photodegradation efficiency decreased drastically. What's more, catalyst dosage is required to be optimized as well to obtain the highest photocatalytic performance.

Evaluating and comparing the catalyst performance require a fundamental understanding of reaction kinetics. Moreover, kinetic analysis serves as a means to validate the proposed mechanisms. The interpretation of photocatalytic system kinetics for water treatment and the elucidation of underlying mechanisms have predominantly relied on Langmuir−Hinshelwood rate laws, which can be simplified to a pseudo-first-order kinetic rate. However, in this study, we assessed four different kinetic models to validate the photodegradation mechanism well. Since each of them has a specific function mechanism, this will aid in determining the nature of the photocatalysts in TC-HCl removal. As shown in Table S3. regarding the pseudo-first-order rate constant ($k_{obs}$ = 0.064 $min^{-1}$) for SNO-ACO-9, the kinetic rate of TC-HCl photodegradation surpasses SNO by 3.5 times and this model fits better to the experimental data than the other three kinetic models listed in Table S3. This discrepancy underscores ACO's significant role in enhancing photocatalytic activity. Prior research on other binary heterojunctions for TC-HCl photocatalytic degradation has demonstrated significantly lower $k_{obs}$ values compared to the value obtained in our study with SNO-ACO-9.[44,45] Collectively, these findings provide compelling evidence that the combination of SNO and ACO represents a promising strategy for crafting an effective photocatalyst for TC-HCl degradation.

To further study the separation and recombination processes of photoexcited charges, photoelectrochemical analysis and characterization tests were implemented. The transient photocurrent of SNO-ACO-9 indicates that it is approximately 3 times higher than that of pristine SNO. Superiority over the photocatalyst individually when subjected to a positive/negative bias voltage (−0.6 V vs Ag/AgCl) indicates that the heterojunction has a higher amount of produced photogenerated electrons and holes and stronger separation.

Incorporating the 3D ACO structure into the SNO nanosheets has several beneficial effects; It leads to electrical resistance reduction and faster charge separation, resulting in improved electron transfer rates. Notably, ACO/SNO-9 exhibits significantly enhanced light absorption compared to pure SNO, particularly in the visible-light range, as shown in Figure 4a. This increased light absorption is attributed to the superior band gap alignment of the materials to absorb


https://doi.org/10.1021/acsestwater.4c00888
ACS EST Water 2025, 5, 351−365

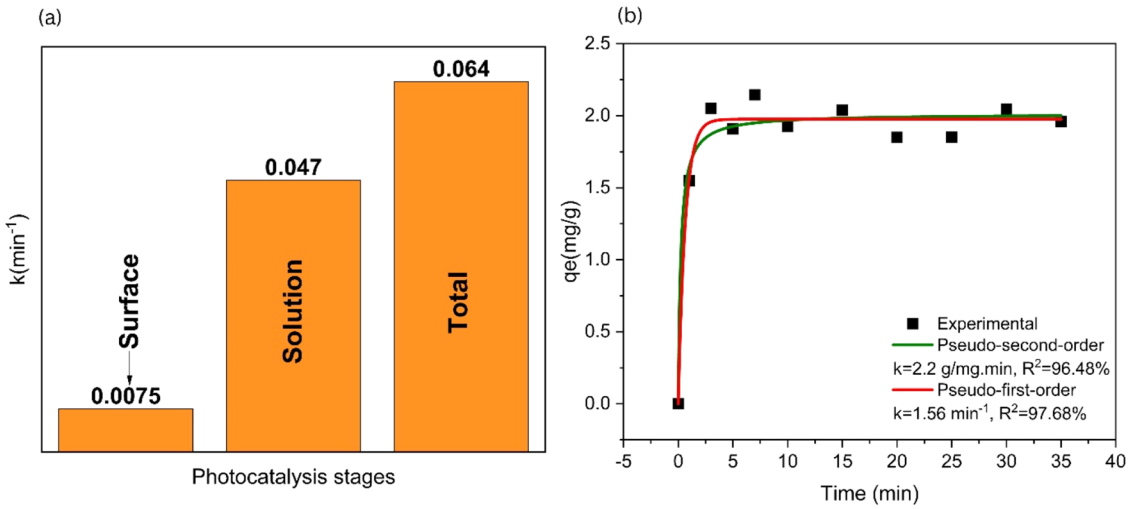


**Figure 5.** TC-HCl removal kinetic rates by different photodegradation processes (a) and adsorption kinetic model fittings (b). The degradation of TC-HCl on the catalyst surface involves adsorption, surface, and solution degradation stages. At pH 5.5, termed "Adsorption + Degradation", an equilibrium adsorption phase precedes photodegradation. Photodegradation at pH 10, with minimal absorption, indicates a significant solution rate ($K_{sol}$) of 0.047 $min^{-1}$, surpassing the surface rate ($K_{sur}$) of 0.0075 $min^{-1}$, highlighting the importance of free radicals. The adsorption kinetic model favors the pseudo-first-order model, with $k_1$ (1.56 $min^{-1}$) surpassing $K_{total}$ (0.064 $min^{-1}$), indicating the enhanced reactivity of the reactive oxygen species (ROS) due to pronounced adsorption, contributing to SNO-ACO-9's exceptional photodegradation performance.

photons and convert them to higher-energy electrons and holes. Consequently, the heterojunction can capture more energy, generating more electron−hole pairs ($e^-$−$h^+$ pairs) and higher electrical current.

Furthermore, the charge transfer superiority of the SNO-ACO-9 junction can be further verified by EIS characterization. The radius of the semicircle in the Nyquist plot obtained from EIS measurements serves as an indicator of the magnitude of resistance during charge transfer within the material. An indication of improved efficiency in charge transfer is denoted by the reduced size of the semicircle. Figure 4d illustrates that the arc diameter of SNO-ACO-9 is smaller compared to that of SNO, suggesting that the addition of ACO at 9% by weight of the mixture reduced the interfacial resistance and enhanced efficiency of electron−hole pair separation and charge transfer within the heterojunction. Additionally, in the Bode-phase spectra depicted in Figure 4c, the decreasing frequency peak of SNO-ACO-9 provides further evidence for the extended electron lifetime, indicating improved charge separation at the interface.

Figure 4b depicts the cyclic voltammograms (CV) of pristine $SnNb_2O_6$ and the $SnNb_2O_6/Ag_2CO_3$ nanocomposite, providing insight into the electrochemical characteristics of the photocatalysts. Both samples exhibit reversible anodic and cathodic peaks (the highlighted area), assigned to the one-electron electrochemical transfer process of the $Fe^{3+}/Fe^{2+}$ couple.[46] Notably, the nanocomposite displays a higher overall area compared to the blank $SnNb_2O_6$ nanosheets, suggesting an augmented electron transfer rate facilitated by the incorporation of ACO with high electrical conductivity. What's more, the nanocomposite illustrates a well-defined $A/A_0$ redox couple (+0.11 V, −0.19 V vs Ag/AgCl) most potentially attributed to the Ag nanoparticles.[47] These results indicate that incorporation of ACO nanoparticles exhibits a distinct redox response compared to bare SNO. By reducing the recombination rate of electron−hole ($e^-$−$h^+$) pairs in ACO/SNO-9, the material exhibits an improved photoelectrochemical performance, resulting in a higher photocurrent density. Altogether, these factors contribute to the enhanced photoelectrochemical capabilities of the junction, making it a promising candidate for efficient photocatalytic applications.

**3.1. Adsorption and Photodegradation Mechanism of TC-HCl.** In general, degradation of the contaminant, herein TC-HCl as the target compound, on the surface of the catalyst is divided into three sections: adsorption, surface, and solution degradation.[48] The overall process involved an equilibrium adsorption phase followed by photodegradation at a pH of 5.5 termed "Adsorption + Degradation". These distinct stages are illustrated in Figure 5a. The photodegradation rate in the condition of pH = 10, in which absorption is in the lowest state, can be accounted for the solution rate ($K_{sol}$) measured to be 0.047 $min^{-1}$, which significantly exceeded that of the surface ($K_{sur}$), 0.0075 $min^{-1}$, affirming more efficient solution photodegradation and the pivotal role of free radicals in the photodegradation process (the surface rate is calculated through the reaction of the photocatalyst and TC-HCl molecules consecutively in TC-HCl solution in dark, ultrapure water in light, and absorption in TC-HCl solution in dark). Figure 5b demonstrates an adsorption kinetic model fitting for the heterojunction photocatalyst. Although the adsorption process appeared to align with both kinetic models, the pseudo-first order kinetic model described the experimental data better in this study. Notably, the value of $K_{ads}$ represented by the the pseudo-first order kinetic coefficient $k_1$ (1.56 $min^{-1}$) was even higher than $K_{total}$ (0.064 $min^{-1}$). This discrepancy signifies that one of the primary factors augmenting the reactivity of the reactive oxygen species (ROS) and enabling the exceptional photodegradation performance of SNO-ACO-9 was its pronounced adsorption effect.

**3.2. Photocatalytic Removal Mechanism.** As commonly recognized, optical absorption characteristics play a crucial role in influencing the photocatalytic performance of a photocatalyst. The UV−visible diffuse reflectance spectra (DRS) for synthesized products are depicted in Figure S6. Since ACO and SNO possess a direct ($n$ = 1/2) band transition, the band


https://doi.org/10.1021/acsestwater.4c00888
ACS EST Water 2025, 5, 351−365

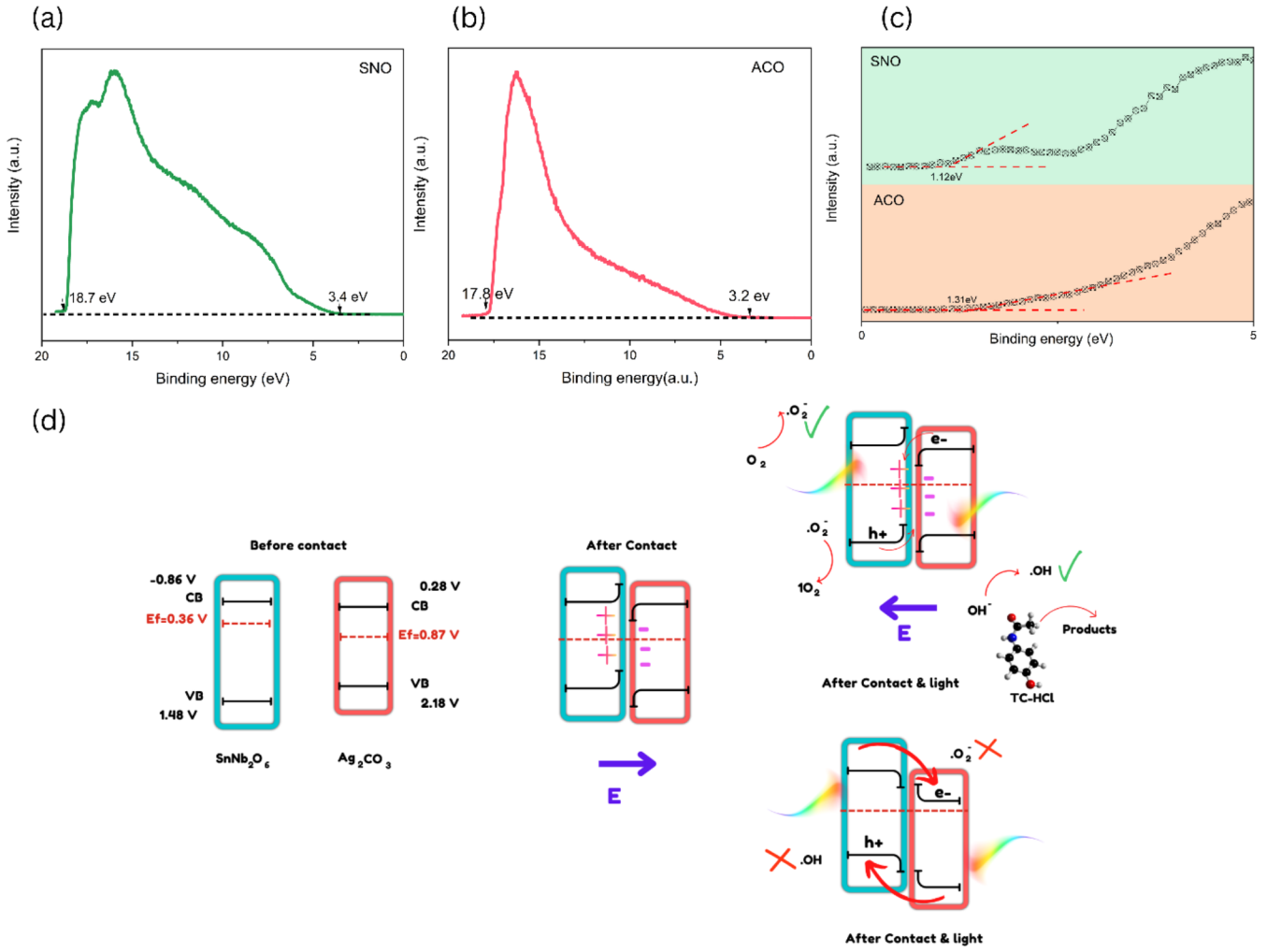


**Figure 6.** UPS spectra of SNO (a), ACO (b), and VB-XPS (c) and the photocatalytic mechanism of Z-scheme SNO-ACO-9% (d).

gap energies can be determined using eq S3.[49] The band gap energies of ACO and SNO are found to be 2.34 and 1.9 eV, respectively, aligning with findings from prior research.[31,32,50] To study the flat band potential ($E_{fb}$) for individual $SnNb_2O_6$ and $Ag_2CO_3$, Mott−Schottky (M−S) analysis was employed. As illustrated in Figure S10, the $E_{fb}$ values for $SnNb_2O_6$ and $Ag_2CO_3$ are assessed at −0.32 and −0.13 V (vs Ag/AgCl), corresponding to −0.12 and 0.07 V (vs NHE). Furthermore, the positive slopes in the M−S plots indicate that both SNO and ACO, as prepared, are n-type semiconductors in nature.

Ultraviolet photoelectron spectroscopy (UPS) analysis is a valuable tool in the determination of the valence band energy of the semiconductors. Valence band energy ($E_{VB}$) determination followed established procedures, involving the subtraction of the He 1 UPS spectra width from the excitation energy (21.22 eV). Consequently, the $E_{VB}$ of SNO was calculated using the formula: $E_{VB} = 21.22 - (18.7 - 3.4) - 4.44 = +1.48$ V, as illustrated in Figure 6a; it is important to note that −4.44 eV vs vacuum level corresponds to 0 V vs NHE. Given the band gap energy of SNO (Figure S6), the $E_{CB}$ of SNO was determined to be −0.86 V using the equation $E_{CB} = E_{VB} - E_g$. Likewise, for ACO (Figure 6b), the $E_{VB}$ and $E_{CB}$ of ACO were calculated to be 2.18 and 0.28 V, respectively. The conduction band edges calculated by this method were approximately close and comparable with the results from the Mott−Schottky plot. Semiconductor Fermi levels were determined through valence band XPS (VB-XPS) analysis. According to the VB-XPS results shown in Figure 6c, the valence band energy versus Fermi level values for SNO and ACO were 1.12[51] and 1.31 eV, respectively. As a result, the Fermi level for SNO (+0.36 V) exceeded that of ACO (+0.87 V). The relative positions of band edges and Fermi levels for the semiconductors are illustrated in Figure 6d. Importantly, the work functions that are correlated directly to the Fermi levels of the two semiconductor photocatalysts significantly influence the redistribution of charges, ultimately establishing an internal electric field. Given that SNO possesses a smaller work function (a higher Femi level potential) than ACO, elctrons started to flow from SNO to ACO, which formed an internal electric field from SNO to ACO after two materials came into contact, until they reached the equilibrium $E_f$ level as also described by Yang et al.[52] Depletion of electrons in SNO and accumulation of them on ACO induced a band edge bending of SNO and ACO (SNO downward band bending and ACO upward band bending), as depicted in Figure 6d. The shaped band bending further restricted the electron flow from SNO to ACO and facilitated a cascadelike mechanism, where photogenerated electrons on ACO were attracted toward photoinduced holes in SNO, leading to their recombination at the interface.[53] This process formed a strong interfacial bond between SNO and ACO, which effectively spares the electrons on the conduction band of SNO and the


https://doi.org/10.1021/acsestwater.4c00888
ACS EST Water 2025, 5, 351−365

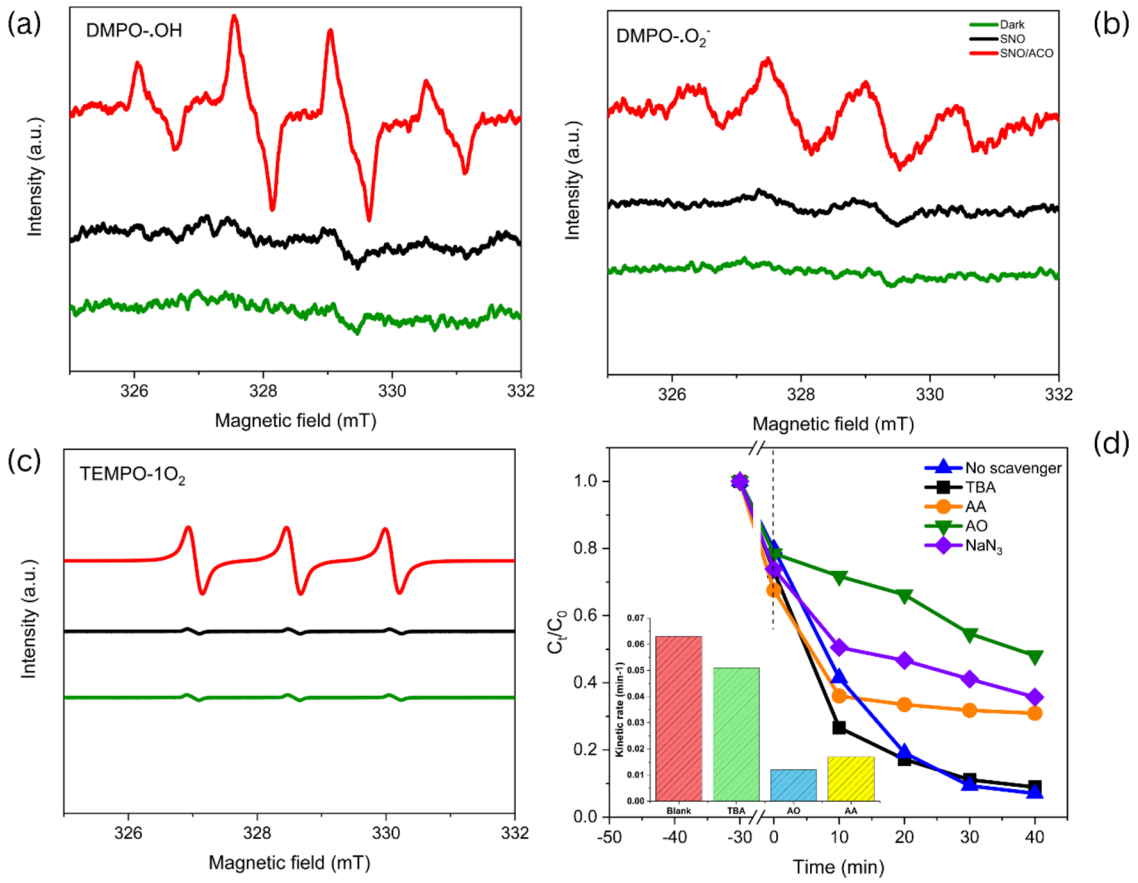


**Figure 7.** ESR spectra of $^{\bullet}OH$ and $^{\bullet}O_2^-$ adducts generated from the reaction of these two radicals with DMPO (a,b), $^1O_2$ adduct produced by TEMPO trapping (c), and the role of reactive species in TC-HCl removal, using various scavengers (the inset figures are the associated degradation rates) (d).

holes on the valence band of ACO. This controlled recombination enhances the photocatalytic efficiency by promoting charge separation, which is essential for driving the desired photocatalytic reactions in the Z-scheme heterojunction system.

The charge transfer mechanism, following the Z-scheme heterojunction model, plays a critical role in driving the desired redox reactions in a heterojunction photocatalysis system. This approach enhances the photocatalytic performance by directing electrons and holes to the appropriate reaction sites for effective oxidative and reductive processes.[54] To elaborate, the accumulation of holes in the valence band of ACO (with a band edge position of 2.18 V) facilitates the production of $^{\bullet}OH$ radicals ($E^{\circ}$ $OH^-/^{\bullet}OH$ = 1.89 V), while electrons gather in the conduction band of SNO (with a band edge of −0.86 V), promoting the production of $^{\bullet}O_2^-$ ($E^{\circ}$ $O_2/^{\bullet}O_2^-$ = −0.18 V). As a result, singlet oxygen, which is the product of $^{\bullet}O_2^-$ oxidation by holes, is also easily generated.[55]

If the charge transfer follows a type II mechanism, photogenerated electrons would accumulate in the conduction band of PC II (ACO in this case), which has a reduction potential lower than that required for $^{\bullet}O_2^-$ production. Simultaneously, holes would accumulate in the valence band of PC I (SNO), which has a weaker oxidation potential than is necessary to generate $^{\bullet}OH$ radicals. This arrangement could reduce the overall driving force for the key photocatalytic reactions. From a dynamic perspective, the electrons already present in PC II generate a repulsive force that impedes the continuous transfer of electrons from PC I, further inhibiting electron transfer from PC I to PC II. Likewise, the repulsion between holes in PC I and those transferred from PC II hinders effective spatial charge separation (Figure 6d). Thus, with the theoretical framework outlined and supported by the experimental results, the Z-scheme charge transfer mechanism of the photogenerated carriers in this proposed system is further validated. This mechanism effectively explains the enhanced performance of heterojunction photocatalysis, as the Z-scheme configuration facilitates efficient charge separation and maximizes the redox potential required for critical photocatalytic reactions.

This charge carrier transfer mechanism was also confirmed by ESR and radical scavenging experiments. As depicted in Figure 7a, four distinct peaks corresponding to DMPO−$^{\bullet}OH$ species in a 1:2:2:1 intensity ratio are observed under light illumination after 8 min. As illustrated in Figure 7a, SNO alone is unable to produce $^{\bullet}OH$ due to its valence band edge position being lower than the $^{\bullet}OH/OH^-$ redox potential (1.89 V) and its poor separation of electrons and holes. However, with the addition of ACO, $^{\bullet}OH$ species are easily generated, reinforcing the Z-scheme charge transfer mechanism and demonstrating a superior charge separation efficiency. This synergistic effect between SNO and ACO further confirms the enhanced photocatalytic activity of the heterojunction system. When using methanol solution, DMPO can capture $^{\bullet}O_2^-$ radicals, forming a characteristic signal of 1:1:1:1 DMPO-$^{\bullet}O_2^-$ quadruple peaks (Figure 7b), indicating the reduction of $O_2$ in


https://doi.org/10.1021/acsestwater.4c00888
ACS EST Water 2025, 5, 351−365

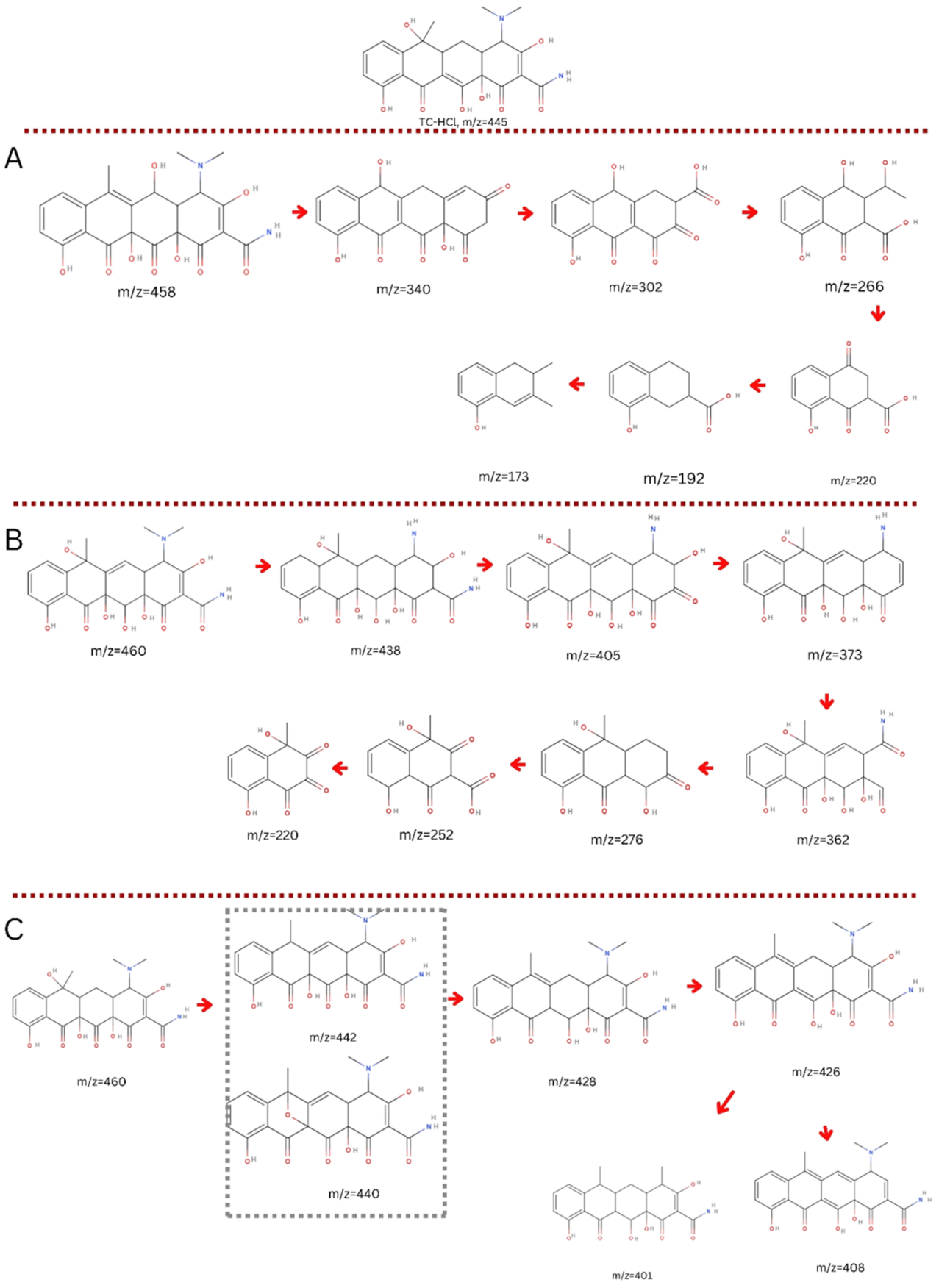


**Figure 8.** continued



https://doi.org/10.1021/acsestwater.4c00888
*ACS EST Water* 2025, 5, 351−365

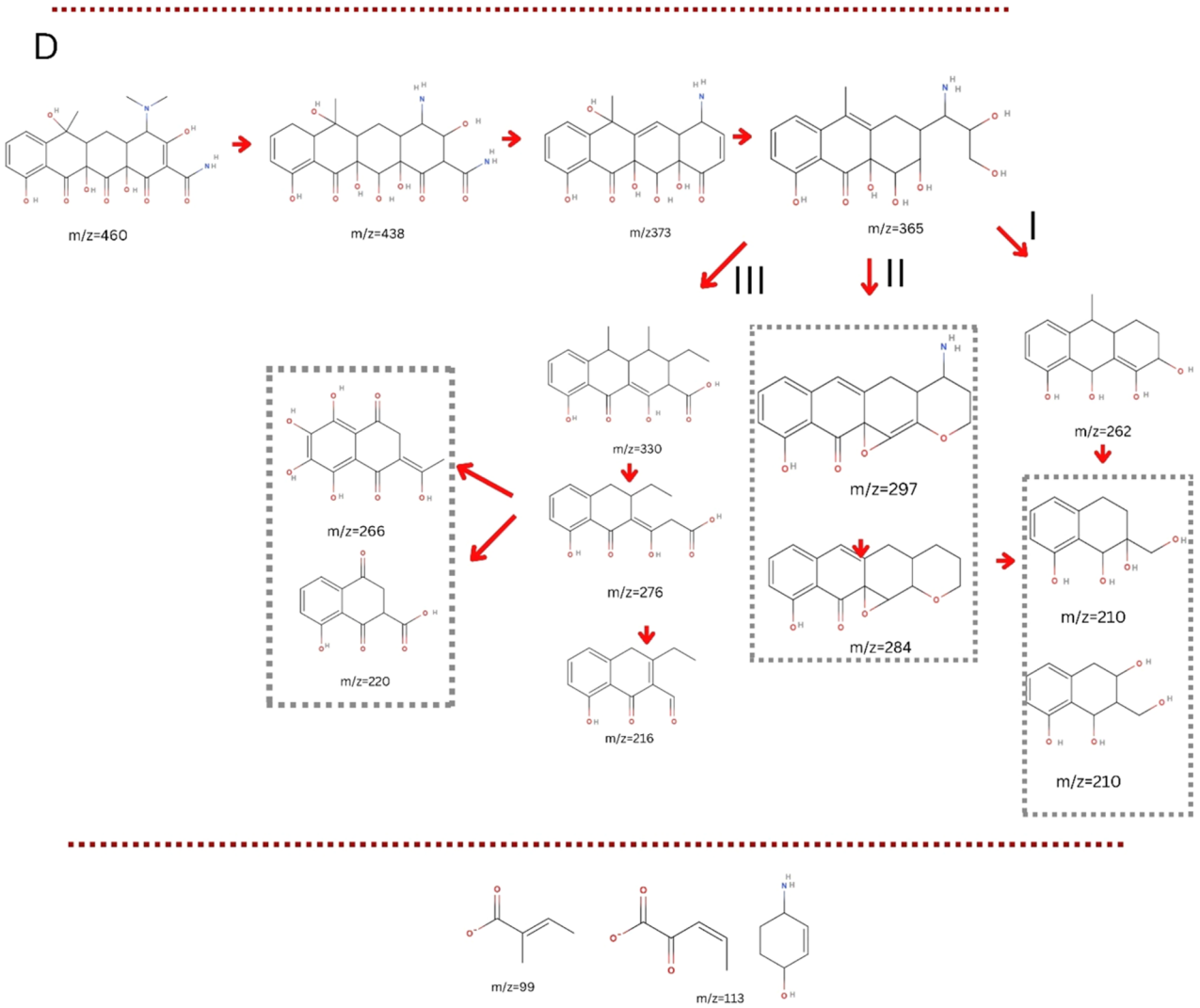


**Figure 8.** Possible degradation pathway of TC-HCl oxidation with the SNO-ACO-9% photocatalyst (A–D).

the solution to $^{\bullet}O_2^-$ by photogenerated electrons. Similarly, in the case of $^{\bullet}O_2^-$ production, the SNO-ACO composite demonstrates improved charge separation, facilitating the generation of a greater quantity of $^{\bullet}O_2^-$ within the system.

Furthermore, in the presence of TEMPO, three peaks of 1:1:1 intensity appear after 8 min under visible light, consistent with the characteristic signal of the TEMPO–$^1O_2$ adduct (Figure 7c), confirming the $^1O_2$ generation through the photocatalysis process. The EPR results align well with radical scavenging experiments, providing confirmation of the production of $^{\bullet}OH$ and $^{\bullet}O_2^-$ radicals by SNO-ACO-9% under visible-light irradiation. To further explore the primary active species generated within the SNO-ACO photocatalytic system and validate the proposed photodegradation system, we conducted quenching experiments using different scavengers, and the outcomes are presented in Figure 7d. Various scavengers, such as ammonium oxalate (AO), tert-butanol (TBA), ascorbic acid (AA), and $NaN_3$, were employed to quench $h^+$, $^{\bullet}OH$, $^{\bullet}O_2^-$, and $^1O_2$, respectively. The inclusion of AO led to a decline in the removal efficiency from 93 to 47%, indicating the prominent role of $h^+$ in degrading TC-HCl. Similarly, a reduction in the degradation efficiency was observed in the presence of AA, suggesting a significant involvement of $^{\bullet}O_2^-$ in TC-HCl degradation. Interestingly, $NaN_3$ and AA exhibited comparable inhibitory effects on the removal efficiency, likely due to the generation of $^1O_2$ from $^{\bullet}O_2^-$. Conversely, slight decreases in the removal efficiency occurred with the addition of TBA, confirming minor contributions of $^{\bullet}OH$ to pollutant degradation in this photocatalytic system. Furthermore, the observed pseudo-first-order rate constants ($k_{obs}$) for TC-HCl photodegradation are 0.017, 0.016, 0.012, and 0.051 $min^{-1}$ when AA, NaN3, AO, and *t*-BuOH are introduced (Figure 7d, inset). This supports the notion that TC primarily undergoes degradation via reactive species such as $^{\bullet}O_2^-$, $^1O_2$, and holes ($h^+$). $^{\bullet}OH$ is making only a minor contribution to the photodegradation process.

As also confirmed by the radical scavenging and ESR experiments, the charge transfer mechanism follows Z-scheme band alignment. Under this assumption, the redox capability of the heterojunction photocatalyst promoted the production of superoxide and hydroxyl radicals as well as singlet oxygen, which were most probably not generated in the type II heterojunction scenario (Figure 6d), therefore improving its photocatalytic activity and TC degradation.

**3.3. Possible Photodegradation Pathway of TC.** To further evaluate the potential process of TC photocatalytic degradation by the SNO/ACO composite, we employed LC-


https://doi.org/10.1021/acsestwater.4c00888
ACS EST Water 2025, 5, 351–365

QTOF to examine the plausible intermediates formed during the photodegradation of TC. Drawing on insights from previous studies and the LC-MS data, 4 conceivable pathways (Figure 8) are proposed for the photodegradation of TC-HCl in the SNO/ACO system.

Pathway A involves the formation of an intermediate with $m/z$ = 458, resulting from several hydroxylation processes, water loss at the second planar ring, and carbon oxidation. This is followed by deamination and dihydroxylation, yielding an intermediate with a $m/z$ = 340. This intermediate undergoes further fragmentation and ring cleavage, producing intermediates with $m/z$ = 302 and $m/z$ = 266. As oxidation progresses, quinonelike structures and smaller molecules, such as $m/z$ = 220, are generated. Subsequent oxidation of these products by potent radicals and reactive species results in two potential structures with $m/z$ = 192 and $m/z$ = 173. These products suggested further oxidation and cleavage of the tetracyclic structure, leaving behind simpler aromatic intermediates such as benzoic acid derivatives.

Pathway B begins with the formation of $m/z$ = 460 through hydroxylation and dehydrogenation. This structure undergoes dealkylation at the amine group and multiple hydrogenation steps, forming $m/z$ = 438, followed by $m/z$ = 405 through hydrogenation, deamination, and decarboxylation. The intermediate $m/z$ = 373 forms due to hydrogenation and hydroxyl loss. Subsequent ring-opening and oxidation lead to the formation of $m/z$ = 362. Further attack by singlet oxygen ($^1O_2$) and hydroxyl radicals ($^\bullet$OH) leads to amine group loss, forming $m/z$ = 276, and smaller molecules such as $m/z$ = 252 and $m/z$ = 220. These smaller breakdown intermediates suggested that the ring structures were opened and transformed into simpler aliphatic or carboxylic acid compounds. The oxidation process continues, further simplifying the molecular structure.

Additionally, TC decomposition can follow Pathway C, where $m/z$ = 460 undergoes either dehydroxylation and hydrogen abstraction, producing $m/z$ = 442, or dehydroxylation with water loss and dehydrogenation, producing $m/z$ = 440. In either case, further oxidation via hydroxyl radical ($^\bullet$OH) attack leads to amine group removal, followed by methylation, forming smaller molecules with $m/z$ = 401. The resulting products suggested that the oxidation process removed critical portions of the original tetracycline molecule, leaving behind an open-ring structure or a smaller polycyclic structure.

Pathway D, the breakdown process from $m/z$ = 460 to $m/z$ = 373, mirrors that of Pathway B. The intermediate then undergoes ring cleavage and hydroxylation, producing $m/z$ = 365. The primary product with $m/z$ = 297 (II) is formed through condensation and dehydration, while $m/z$ = 330 (III) is produced by the removal of side groups such as amine and hydroxyl groups, followed by carboxylation. Further oxidation of these compounds results in smaller molecules with $m/z$ = 276, 216, and 210. Meanwhile, along this pathway, some quinonelike structures could also be produced ($m/z$ = 266, $m/z$ = 220) as smaller intermediates. Ultimately, all intermediates undergo a complete breakdown into $CO_3^{2-}$, $H_2O$, and $NH_4^+$.

## CONCLUSIONS

To summarize, we formulated and engineered an innovative binary Z-scheme photocatalyst, composed of SNO-ACO, without any need for a third agent as the charge mediator. We showed that the synthesized materials, when exposed to visible light, exhibited promising photocatalytic proficiency in environmental application as pharmaceutical removal, and the study revealed that incorporating ACO in the mixture with a low mass ratio of 9% can increase the TC-HCl removal kinetic rate from 0.019 to 0.064 $min^{-1}$. Moreover, we showed that photodegradation of the pollutant by the photocatalysis project is divided mainly into three sections: adsorption, surface degradation, and solution degradation. In the case of our binary heterojunction, solution degradation came to prominence, which intensified the effect of free radicals and ROS in the solution. In addition, studying the nature of the transfer mechanism of the material, incorporating findings from radical scavenging tests, ESR signals, UPS, VB-XPS, and DRS measurements, it is evident that the charge transfer mechanism in the SNO-ACO heterostructure is characterized by a Z-type configuration, as opposed to the conventional type II heterojunction charge transfer mechanism. Unlike conventional heterojunctions, this binary Z-scheme heterojunction, characterized by robust internal interactions between the two semiconductors in the binary composite, accounted for a heightened redox potential, efficient separation of charge carriers, augmented visible-light reactivity, and enhanced photocatalytic efficacy.

## ASSOCIATED CONTENT

### Supporting Information

The Supporting Information is available free of charge at https://pubs.acs.org/doi/10.1021/acsestwater.4c00888.

SEM images of the photocatalysts; HRTEM images of SNO nanosheets; effect of photocatalyst dosage on TC photodegradation; measured parameters for SNO and the heterostructure; effect of water matrix parameters on TC degradation; and comparison of Z-scheme photocatalysts reported in literature with the current study (PDF)

## AUTHOR INFORMATION


### Corresponding Author

**Jiangyong Hu** − *Department of Civil and Environmental Engineering, National University of Singapore, 117576, Singapore;* orcid.org/0000-0002-6467-2805; Email: ceehujy@nus.edu.sg

### Authors

**Zahra Beiramzadeh** − *Department of Civil and Environmental Engineering, National University of Singapore, 117576, Singapore*

**Mohammad Tanhaei** − *P&E Department, Faculty of Mechanical Engineering, Delft University of Technology, 2628 CD Delft, The Netherlands;* orcid.org/0000-0002-0663-5969

**Yixiang Li** − *Pillar of Engineering Product Development, Singapore University of Technology and Design, Singapore 487372, Singapore*

**Hui Ying Yang** − *Pillar of Engineering Product Development, Singapore University of Technology and Design, Singapore 487372, Singapore;* orcid.org/0000-0002-2244-8231

Complete contact information is available at: https://pubs.acs.org/10.1021/acsestwater.4c00888


### Notes

The authors declare no competing financial interest.



https://doi.org/10.1021/acsestwater.4c00888
ACS EST Water 2025, 5, 351−365

## ■ ACKNOWLEDGMENTS

Z.B. expresses gratitude to the Agency for Science, Technology, and Research (A*STAR) for awarding the SINGA graduate scholarship. The authors also appreciate the support received from the Center for Water Research (CWR) of the National University of Singapore (NUS).

## ■ REFERENCES

(1) Chen, L.; Yang, S.; Huang, Y.; Zhang, B.; Kang, F.; Ding, D.; Cai, T. Degradation of Antibiotics in Multi-Component Systems with Novel Ternary AgBr/Ag3PO4@ Natural Hematite Heterojunction Photocatalyst under Simulated Solar Light. *J. Hazard. Mater.* **2019**, *371*, 566−575.

(2) Yang, Y.-Y.; Zhang, X.-G.; Niu, C.-G.; Feng, H.-P.; Qin, P.-Z.; Guo, H.; Liang, C.; Zhang, L.; Liu, H.-Y.; Li, L. Dual-Channel Charges Transfer Strategy with Synergistic Effect of Z-Scheme Heterojunction and LSPR Effect for Enhanced Quasi-Full-Spectrum Photocatalytic Bacterial Inactivation: New Insight into Interfacial Charge Transfer and Molecular Oxygen Activation. *Appl. Catal., B* **2020**, *264*, No. 118465.

(3) Binh, V. N.; Dang, N.; Anh, N. T. K.; Ky, L. X.; Thai, P. K. Antibiotics in the Aquatic Environment of Vietnam: Sources, Concentrations, Risk and Control Strategy. *Chemosphere* **2018**, *197*, 438−450.

(4) Yuan, Z.; Sui, M.; Yuan, B.; Li, P.; Wang, J.; Qin, J.; Xu, G. Degradation of Ibuprofen Using Ozone Combined with Peroxymonosulfate. *Environ. Sci. Water Res. Technol.* **2017**, *3* (5), 960−969.

(5) Wang, S.; Wang, J. Comparative Study on Sulfamethoxazole Degradation by Fenton and Fe (II)-Activated Persulfate Process. *RSC Adv.* **2017**, *7* (77), 48670−48677.

(6) Liu, H.-Y.; Niu, C.-G.; Guo, H.; Liang, C.; Huang, D.-W.; Zhang, L.; Yang, Y.-Y.; Li, L. In Suit Constructing 2D/1D MgIn2S4/CdS Heterojunction System with Enhanced Photocatalytic Activity towards Treatment of Wastewater and H2 Production. *J. Colloid Interface Sci.* **2020**, *576*, 264−279.

(7) Liang, C.; Niu, C.-G.; Zhang, L.; Wen, X.-J.; Yang, S.-F.; Guo, H.; Zeng, G.-M. Construction of 2D Heterojunction System with Enhanced Photocatalytic Performance: Plasmonic Bi and Reduced Graphene Oxide Co-Modified Bi5O7I with High-Speed Charge Transfer Channels. *J. Hazard. Mater.* **2019**, *361*, 245−258.

(8) Kim, Y. G.; Jo, W.-K. Efficient Decontamination of Textile Industry Wastewater Using a Photochemically Stable n−n Type CdSe/Ag3PO4 Heterostructured Nanohybrid Containing Metallic Ag as a Mediator. *J. Hazard. Mater.* **2019**, *361*, 64−72.

(9) Li, B.; Liu, S.; Lai, C.; Zeng, G.; Zhang, M.; Zhou, M.; Huang, D.; Qin, L.; Liu, X.; Li, Z.; et al. Unravelling the Interfacial Charge Migration Pathway at Atomic Level in 2D/2D Interfacial Schottky Heterojunction for Visible-Light-Driven Molecular Oxygen Activation. *Appl. Catal., B* **2020**, *266*, No. 118650.

(10) Zhou, C.; Lai, C.; Huang, D.; Zeng, G.; Zhang, C.; Cheng, M.; Hu, L.; Wan, J.; Xiong, W.; Wen, M.; et al. Highly Porous Carbon Nitride by Supramolecular Preassembly of Monomers for Photocatalytic Removal of Sulfamethazine under Visible Light Driven. *Appl. Catal., B* **2018**, *220*, 202−210.

(11) Jia, T.; Wu, J.; Song, J.; Liu, Q.; Wang, J.; Qi, Y.; He, P.; Qi, X.; Yang, L.; Zhao, P. In Situ Self-Growing 3D Hierarchical BiOBr/BiOIO3 Z-Scheme Heterojunction with Rich Oxygen Vacancies and Iodine Ions as Carriers Transfer Dual-Channels for Enhanced Photocatalytic Activity. *Chem. Eng. J.* **2020**, *396*, No. 125258.

(12) Qu, Y.; Liao, L.; Cheng, R.; Wang, Y.; Lin, Y.-C.; Huang, Y.; Duan, X. Rational Design and Synthesis of Freestanding Photoelectric Nanodevices as Highly Efficient Photocatalysts. *Nano Lett.* **2010**, *10* (5), 1941−1949.

(13) Zhao, G.; Ding, J.; Zhou, F.; Chen, X.; Wei, L.; Gao, Q.; Wang, K.; Zhao, Q. Construction of a Visible-Light-Driven Magnetic Dual Z-Scheme BiVO4/g-C3N4/NiFe2O4 Photocatalyst for Effective Removal of Ofloxacin: Mechanisms and Degradation Pathway. *Chem. Eng. J.* **2021**, *405*, No. 126704.

(14) Zhao, W.; Feng, Y.; Huang, H.; Zhou, P.; Li, J.; Zhang, L.; Dai, B.; Xu, J.; Zhu, F.; Sheng, N.; Leung, D. Y. A Novel Z-Scheme Ag3VO4/BiVO4 Heterojunction Photocatalyst: Study on the Excellent Photocatalytic Performance and Photocatalytic Mechanism. *Appl. Catal., B* **2019**, *245*, 448−458.

(15) Guo, H.; Niu, C.-G.; Zhang, L.; Wen, X.-J.; Liang, C.; Zhang, X.-G.; Guan, D.-L.; Tang, N.; Zeng, G.-M. Construction of Direct Z-Scheme AgI/Bi2Sn2O7 Nanojunction System with Enhanced Photocatalytic Activity: Accelerated Interfacial Charge Transfer Induced Efficient Cr (VI) Reduction, Tetracycline Degradation and *Escherichia coli* Inactivation. *ACS Sustainable Chem. Eng.* **2018**, *6* (6), 8003−8018.

(16) Li, H.; Tu, W.; Zhou, Y.; Zou, Z. Z-Scheme Photocatalytic Systems for Promoting Photocatalytic Performance: Recent Progress and Future Challenges. *Adv. Sci.* **2016**, *3* (11), No. 1500389.

(17) Ding, J.; Dai, Z.; Qin, F.; Zhao, H.; Zhao, S.; Chen, R. Z-Scheme BiO1-XBr/Bi2O2CO3 Photocatalyst with Rich Oxygen Vacancy as Electron Mediator for Highly Efficient Degradation of Antibiotics. *Appl. Catal., B* **2017**, *205*, 281−291.

(18) Jiang, D.; Ma, W.; Xiao, P.; Shao, L.; Li, D.; Chen, M. Enhanced Photocatalytic Activity of Graphitic Carbon Nitride/Carbon Nanotube/Bi2WO6 Ternary Z-Scheme Heterojunction with Carbon Nanotube as Efficient Electron Mediator. *J. Colloid Interface Sci.* **2018**, *512*, 693−700.

(19) Ghosh, U.; Pal, A. Fabrication of a Novel Bi2O3 Nanoparticle Impregnated Nitrogen Vacant 2D G-C3N4 Nanosheet Z Scheme Photocatalyst for Improved Degradation of Methylene Blue Dye under LED Light Illumination. *Appl. Surf. Sci.* **2020**, *507*, No. 144965.

(20) Hosogi, Y.; Shimodaira, Y.; Kato, H.; Kobayashi, H.; Kudo, A. Role of Sn2+ in the Band Structure of SnM2O6 and Sn2M2O7 (M= Nb and Ta) and Their Photocatalytic Properties. *Chem. Mater.* **2008**, *20* (4), 1299−1307.

(21) Samizo, A.; Kikuchi, N.; Aiura, Y.; Nishio, K.; Mibu, K. Carrier Generation in P-Type Wide-Gap Oxide: SnNb2O6 Foordite. *Chem. Mater.* **2018**, *30* (22), 8221−8225.

(22) Cruz, L. P.; Savariault, J.-M.; Rocha, J.; Jumas, J.-C.; De Jesus, J. D. P. Synthesis and Characterization of Tin Niobates. *J. Solid State Chem.* **2001**, *156* (2), 349−354.

(23) Hosogi, Y.; Kato, H.; Kudo, A. Synthesis of SnNb2O6 Nanoplates and Their Photocatalytic Properties. *Chem. Lett.* **2006**, *35* (6), 578−579.

(24) Ma, X.; Ma, W.; Jiang, D.; Li, D.; Meng, S.; Chen, M. Construction of Novel WO3/SnNb2O6 Hybrid Nanosheet Heterojunctions as Efficient Z-Scheme Photocatalysts for Pollutant Degradation. *J. Colloid Interface Sci.* **2017**, *506*, 93−101.

(25) Jiang, R.; Lu, G.; Yan, Z.; Wu, D.; Zhou, R.; Bao, X. Insights into a CQD-SnNb2O6/BiOCl Z-Scheme System for the Degradation of Benzocaine: Influence Factors, Intermediate Toxicity and Photocatalytic Mechanism. *Chem. Eng. J.* **2019**, *374*, 79−90.

(26) Wen, X.-J.; Niu, C.-G.; Guo, H.; Zhang, L.; Liang, C.; Zeng, G.-M. Photocatalytic Degradation of Levofloxacin by Ternary Ag2CO3/CeO2/AgBr Photocatalyst under Visible-Light Irradiation: Degradation Pathways, Mineralization Ability, and an Accelerated Interfacial Charge Transfer Process Study. *J. Catal.* **2018**, *358*, 211−223.

(27) Li, L.; Niu, C.-G.; Guo, H.; Wang, J.; Ruan, M.; Zhang, L.; Liang, C.; Liu, H.-Y.; Yang, Y.-Y. Efficient Degradation of Levofloxacin with Magnetically Separable ZnFe2O4/NCDs/Ag2CO3 Z-Scheme Heterojunction Photocatalyst: Vis-NIR Light Response Ability and Mechanism Insight. *Chem. Eng. J.* **2020**, *383*, No. 123192.

(28) Liu, Y.; Kong, J.; Yuan, J.; Zhao, W.; Zhu, X.; Sun, C.; Xie, J. Enhanced Photocatalytic Activity over Flower-like Sphere Ag/Ag2CO3/BiVO4 Plasmonic Heterojunction Photocatalyst for Tetracycline Degradation. *Chem. Eng. J.* **2018**, *331*, 242−254.

(29) Liu, H.-Y.; Liang, C.; Niu, C.-G.; Huang, D.-W.; Du, Y.-B.; Guo, H.; Zhang, L.; Yang, Y.-Y.; Zeng, G.-M. Facile Assembly of G-C3N4/Ag2CO3/Graphene Oxide with a Novel Dual Z-Scheme System for Enhanced Photocatalytic Pollutant Degradation. *Appl. Surf. Sci.* **2019**, *475*, 421−434.



https://doi.org/10.1021/acsestwater.4c00888
*ACS EST Water* 2025, 5, 351−365

(30) Wu, W.; Xuan, Y.; Jin, Y.; Liang, X.; Meng, S.; Chen, M. Construction of Novel CdS/SnNb2O6 Heterojunctions with Enhanced Photocatalytic Degradation Activity Under Visible Light. *Eur. J. Inorg. Chem.* **2018**, *2018* (44), 4812−4818.
(31) Chen, Z.-J.; Guo, H.; Liu, H.-Y.; Niu, C.-G.; Huang, D.-W.; Yang, Y.-Y.; Liang, C.; Li, L.; Li, J.-C. Construction of Dual S-Scheme Ag2CO3/Bi4O5I2/g-C3N4 Heterostructure Photocatalyst with Enhanced Visible-Light Photocatalytic Degradation for Tetracycline. *Chem. Eng. J.* **2022**, *438*, No. 135471.
(32) Luo, B.; Hong, Y.; Li, D.; Fang, Z.; Jian, Y.; Shi, W. Fabrication of 0D/2D Carbon Nitride Quantum Dots/SnNb2O6 Ultrathin Nanosheets with Enhanced Photocatalytic Hydrogen Production. *ACS Sustainable Chem. Eng.* **2018**, *6* (11), 14332−14339.
(33) Low, J.; Jiang, C.; Cheng, B.; Wageh, S.; Al-Ghamdi, A. A.; Yu, J. A Review of Direct Z-scheme Photocatalysts. *Small Methods* **2017**, *1* (5), No. 1700080.
(34) Yuan, X.; Jiang, L.; Chen, X.; Leng, L.; Wang, H.; Wu, Z.; Xiong, T.; Liang, J.; Zeng, G. Highly Efficient Visible-Light-Induced Photoactivity of Z-Scheme Ag 2 CO 3/Ag/WO 3 Photocatalysts for Organic Pollutant Degradation. *Environ. Sci. Nano* **2017**, *4* (11), 2175−2185.
(35) Xu, J.; Liu, Y.; Chen, M. Construction of SnNb 2 O 6/MgIn 2 S 4 Heterojunction Photocatalysts with Enhanced Visible-Light-Driven Activity for Tetracycline Hydrochloride Degradation and Cr (vi) Reduction. *Catal. Sci. Technol.* **2022**, *12* (7), 2328−2339.
(36) Reddy, P. N.; Sreedhar, A.; Reddy, M. H. P.; Uthanna, S.; Pierson, J. F. The Effect of Oxygen Partial Pressure on Physical Properties of Nano-crystalline Silver Oxide Thin Films Deposited by RF Magnetron Sputtering. *Cryst. Res. Technol.* **2011**, *46* (9), 961−966.
(37) Rahman, T.; Martin, N. P.; Jenkins, J. K.; Elzein, R.; Fast, D. B.; Addou, R.; Herman, G. S.; Nyman, M. Nb2O5, LiNbO3, and (Na, K) NbO3 Thin Films from High-Concentration Aqueous Nb-Polyoxometalates. *Inorg. Chem.* **2022**, *61* (8), 3586−3597.
(38) Tang, H.; Chang, S.; Tang, G.; Liang, W. AgBr and G-C3N4 Co-Modified Ag2CO3 Photocatalyst: A Novel Multi-Heterostructured Photocatalyst with Enhanced Photocatalytic Activity. *Appl. Surf. Sci.* **2017**, *391*, 440−448.
(39) Su, X.; Wang, A.; Xu, L.; Zhang, W.; Guo, F.; Zhang, D.; Pu, X.; Cai, P. Low-temperature Synthesis One-dimensional Ag2CO3/SnFe2O4 Z-scheme with Excellent Visible-light Photoactivity. *J. Am. Ceram. Soc.* **2023**, *106* (6), 3594−3604.
(40) Li, X.; Garlisi, C.; Guan, Q.; Anwer, S.; Al-Ali, K.; Palmisano, G.; Zheng, L. A Review of Material Aspects in Developing Direct Z-Scheme Photocatalysts. *Mater. Today* **2021**, *47*, 75−107.
(41) Ramar, V.; Balasubramanian, K. Reduced Graphene Oxide/WO3 Nanorod Composites for Photocatalytic Degradation of Methylene Blue under Sunlight Irradiation. *ACS Appl. Nano Mater.* **2021**, *4* (5), 5512−5521.
(42) Gu, C.; Karthikeyan, K. G. Interaction of Tetracycline with Aluminum and Iron Hydrous Oxides. *Environ. Sci. Technol.* **2005**, *39* (8), 2660−2667.
(43) Adorna, J., Jr; Annadurai, T.; Bui, T. A. N.; Tran, H. L.; Lin, L.-Y.; Doong, R.-A. Indirect Z-Scheme Nitrogen-Doped Carbon Dot Decorated Bi2MoO6/g-C3N4 Photocatalyst for Enhanced Visible-Light-Driven Degradation of Ciprofloxacin. *Chem. Eng. J.* **2021**, *422*, No. 130103.
(44) Huang, D.; Li, J.; Zeng, G.; Xue, W.; Chen, S.; Li, Z.; Deng, R.; Yang, Y.; Cheng, M. Facile Construction of Hierarchical Flower-like Z-Scheme AgBr/Bi2WO6 Photocatalysts for Effective Removal of Tetracycline: Degradation Pathways and Mechanism. *Chem. Eng. J.* **2019**, *375*, No. 121991.
(45) Zhou, C.; Lai, C.; Xu, P.; Zeng, G.; Huang, D.; Li, Z.; Zhang, C.; Cheng, M.; Hu, L.; Wan, J.; et al. Rational Design of Carbon-Doped Carbon Nitride/Bi12O17Cl2 Composites: A Promising Candidate Photocatalyst for Boosting Visible-Light-Driven Photocatalytic Degradation of Tetracycline. *ACS Sustainable Chem. Eng.* **2018**, *6* (5), 6941−6949.
(46) Yuan, L.; Yang, M.-Q.; Xu, Y.-J. Tuning the Surface Charge of Graphene for Self-Assembly Synthesis of a SnNb 2 O 6 Nanosheet−Graphene (2D−2D) Nanocomposite with Enhanced Visible Light Photoactivity. *Nanoscale* **2014**, *6* (12), 6335−6345.
(47) Van der Horst, C.; Silwana, B.; Iwuoha, E.; Somerset, V. Synthesis and Characterization of Bismuth-Silver Nanoparticles for Electrochemical Sensor Applications. *Anal. Lett.* **2015**, *48* (8), 1311−1332.
(48) Gao, B.; Pan, Y.; Chang, Q.; Xi, Z.; Yang, H. Hierarchically Z-Scheme Photocatalyst of {0 1 0} BiVO4/Ag/CdS with Enhanced Performance in Synergistic Adsorption-Photodegradation of Fluoroquinolones in Water. *Chem. Eng. J.* **2022**, *435*, No. 134834.
(49) Wang, B.; Liu, Y.; Huang, Z.; Fang, M. Energy Transfer and Thermal Stability of Ce3+, Tb3+ Co-Doped Ca3Si2O4N2 Phosphors for White Light-Emitting Diodes. *Chem. Phys. Lett.* **2017**, *690*, 31−37.
(50) Jin, Y.; Jiang, D.; Li, D.; Xiao, P.; Ma, X.; Chen, M. SrTiO3 Nanoparticle/SnNb2O6 Nanosheet 0D/2D Heterojunctions with Enhanced Interfacial Charge Separation and Photocatalytic Hydrogen Evolution Activity. *ACS Sustainable Chem. Eng.* **2017**, *5* (11), 9749−9757.
(51) Katayama, S.; Hayashi, H.; Kumagai, Y.; Oba, F.; Tanaka, I. Electronic Structure and Defect Chemistry of Tin (II) Complex Oxide SnNb2O6. *J. Phys. Chem. C* **2016**, *120* (18), 9604−9611.
(52) Yang, Y.-Y.; Guo, H.; Huang, D.-W.; Li, L.; Liu, H.-Y.; Sui, L.; Wu, Q.; Zhu, J.-J.; Zhang, L.; Niu, C.-G. Simultaneously Tuning Oxygen Reduction Pathway and Charge Transfer Dynamics toward Sacrificial Agent-Free Photocatalytic H2O2 Production for in-Situ Water Disinfection. *Chem. Eng. J.* **2024**, *479*, No. 147863.
(53) Yang, Y.-Y.; Feng, H.-P.; Zhang, X.-G.; Guo, H.; Wen, X.-J.; Sui, L.; Dong, Z.-T.; Yan, M.; Niu, C.-G. Regulating and Protecting of Oxygen Vacancy Endow MoO3-X@ Zn2In2S5 S-Scheme Core−Shell Heterojunction with High-Efficiency Organic Pollutant Removal and Bacterial Disinfection: Correlation of Pollutant Active Sites to Degradation Pathways. *Chem. Eng. J.* **2024**, *490*, No. 151309.
(54) Liu, H.-Y.; Niu, C.-G.; Huang, D.-W.; Liang, C.; Guo, H.; Yang, Y.-Y.; Li, L. Unravelling the Role of Reactive Oxygen Species in Ultrathin Z-Scheme Heterojunction with Surface Zinc Vacancies for Photocatalytic H2O2 Generation and CTC Degradation. *Chem. Eng. J.* **2023**, *465*, No. 143007.
(55) Fan, Q.-Q.; Niu, C.-G.; Guo, H.; Huang, D.-W.; Dong, Z.-T.; Yang, Y.-Y.; Liu, H.-Y.; Li, L.; Qin, M.-Z. Insights into the Role of Reactive Oxygen Species in Photocatalytic H2O2 Generation and OTC Removal over a Novel BN/Zn3In2S6 Heterojunction. *J. Hazard. Mater.* **2022**, *438*, No. 129483.


https://doi.org/10.1021/acsestwater.4c00888
*ACS EST Water* 2025, 5, 351−365